The Diversity of Type Ia Supernovae from Broken Symmetries

Daniel Kasen[1,2], F. K. Röpke[3], & S. E. Woosley[1]

[1] *Department of Astronomy and Astrophysics, UCSC, Santa Cruz CA, 95064, USA*

[2] *Hubble Fellow*

[2]*Max Planck Institut für Astrophysik, Karl-Schwarzschild-Str. 1, D-85741 Garching, Germany*

Type Ia supernovae result when carbon-oxygen white dwarfs in binary systems accrete mass from companion stars, reach a critical mass, and explode. The near uniformity of their light curves makes these supernova good standard candles for measuring cosmic expansion[1,2,3,4], but a correction must be applied to account for the fact that the brighter supernovae have broader light curves[5]. One-dimensional modelling, with a certain choice of parameters, can reproduce this general trend in the width-luminosity relation[6,7,8], but the processes of ignition and detonation have recently been shown to be intrinsically asymmetric[9,10,11,12,13]. Here we report on multi-dimensional modelling of the explosion physics and radiative transfer that reveals that the breaking of spherical symmetry is a critical factor in determining both the width luminosity relation and the observed scatter about it. The deviation from sphericity can also explain the finite polarization detected in the light from some supernovae[14]. The slope and normalization of the width-luminosity relation has a weak dependence on certain properties of the white dwarf progenitor, in particular the trace abundances of elements other than carbon and oxygen. Failing to correct for this effect could lead to systematic overestimates of up to 2% in the distance to remote supernovae.

In the most established model for SNe Ia, a carbon fusion flame is ignited near the center of the white dwarf and initially burns in a sub-sonic and turbulent deflagration, then transitions near the white dwarf surface to a supersonic detonation[15,16]. The detonation is needed in order to match the observed energetics and nucleosynthesis[17]. The energetic stage of the explosion lasts only a second or so, but synthesizes radioactive ^{56}Ni that powers the subsequent light curve and determines its luminosity. In previous 1-dimensional models, the ^{56}Ni yield depended on the choices of parameters representing the speed of the subsonic burning front and the density at which the front makes a transition to a detonation wave[18]. However, these parameters are actually a consequence of multi-dimensional instabilities not captured in 1D, and so were not highly constrained by physics. Ignition in the 1D models also occurred at the very center of the star, and the transition to detonation happened simultaneously on a symmetric spherical shell. Both of these assumptions are now doubted.

The starting point of our simulations is a standard 1.38 solar mass white dwarf composed of 50% carbon and 50% oxygen with a central density of 2.9×10^9 g cm^{-3}. The propagation of the burning is followed in 2 spatial dimensions using a level set to track the flame's location and a turbulent subgrid model adopted from the chemical combustion community to describe its motion[12]. The resulting debris are then post-processed using a multi-dimensional radiative transport code[19] to determine the emergent radiation. Model variations consist of how the white dwarf is ignited and the criteria for making the transition to detonation, both of which are based on insights from recent 3-D studies, as described below. Variations in the trace abundance of elements other than carbon/oxygen (the metallicity) of the progenitor star over a range from 1/3 to 3 times solar are also explored to mimic the evolution in supernova environment that may have occurred over aeons of cosmic time.

Simulations show[9,20] that just prior to ignition the white dwarf undergoes a simmer phase characterized by dipolar convection, with material flowing out of the center in a directed plume then circulating back in through the opposite side. The hottest points in the flow, and therefore where ignition occurs, are found on one side of the star displaced slightly from the center. As the simulations have been computed at much lower Reynolds number (~1,000) than the true star (~10^{14}), the real flow may be even less ordered, retaining a dipole flavor but contaminated by higher multipoles, making ignition a much more chaotic process. The geometry of ignition may also be influenced by the rotation rate of the star. In our models we therefore varied the number of ignition points, their distance from the center of the star, and the solid angle in which they were distributed.

The physics of a putative transition to detonation, though still uncertain, has also been elucidated in recent studies[21,22,23]. As the deflagration flame propagates into lower density material, it thickens and slows to the point that turbulent eddies can mix hot fuel and cold ash, causing the burning rate to become highly irregular and potentially explosive. Like ignition, detonation should be a stochastic process which occurs only for the most extreme and intermittent turbulent energies, and may occur many times in different places. We therefore varied the criteria (critical Karlovitz number) for instituting a detonation (see supplementary material).

Fig. 1 shows the final chemical structure (100 seconds after ignition) of the stellar debris for a sample of models. The inner regions of material, which were burned primarily in the turbulent, Rayleigh-Taylor unstable deflagration phase, consist of a patchy mixture of ^{56}Ni, intermediate mass elements (IMEs), and stable iron-group isotopes produced by electron capture (mostly ^{54}Fe and ^{58}Ni),. The subsequent detonation produced a smoother distribution of IMEs in the outer layers of the star. The synthetic

model light curves, colors, and spectral time series agree very well with those of real events observed over the two months after explosion[24] (Figure 2), offering a strong validation of the model's predicted velocity structure and chemical stratification. On the other hand, it has been suggested that the mixing of electron capture elements throughout the inner layers - a feature generic to all multi-dimensional deflagration calculations - may be inconsistent with spectral observations of some SNe Ia taken at late phases[25].

The models predict a range of ^{56}Ni yields, from 0.3 to 1.1 solar masses, depending on the initial conditions. Perhaps counter-intuitively, models with more robust ignition generally synthesize less ^{56}Ni. A strong ignition (i.e., numerous, symmetrically distributed sparks) increases the amount of burning in the deflagration phase during which the star expands and the density declines. This reduces the ^{56}Ni produced in the subsequent detonation wave. A weak or asymmetrical ignition, on the other hand, gives little deflagration burning and minimal pre-expansion, so that the detonation synthesizes abundant ^{56}Ni. For similar reasons, the ^{56}Ni mass also depended on the detonation criteria, as noted in previous 1-D calculations[18].

Given the range in ^{56}Ni masses, the model peak luminosities vary by a factor of 3, from 0.7 to 2.1 x 10^{43} erg s^{-1} which spans the range of normal SNe Ia, though does not reproduce the more extreme and peculiar sub- and super-luminous events[26]. A substantial amount of the dispersion in SN Ia luminosities may therefore be the result of the stochastic and asymmetrical nature of the explosion itself, aside from any variations in the properties of the progenitor star. The rms dispersion in brightness depends on the wavelength band considered, being 45% in the blue, 27% in the red, and only 21% in the near infrared (~1.25 um). This reflects a self-regulating property of the radiative transfer -- dimmer models are relatively cooler, and so radiate a greater percentage of their flux at

longer wavelengths. The models thus confirm observational indications that SNe Ia are nearly standard (as opposed to merely standardizable) candles in the near infrared[27].

Without introducing any artificial tuning, the luminosity of the models correlates with the light curve decline rate, giving a width-luminosity-relation (WLR) similar to that observed (Fig. 3). A correlation is also found between brightness and the color measured at peak. The rms scatter in the model WLR alone is 24%, while using both decline rate and color reduces the dispersion to 21% -- similar to, but slightly greater than ~16% that is observed[28]. The larger diversity seen in the models suggests that additional important physics may constrain the ignition and detonation conditions to a range narrower than that considered here. As in observations, the calibration of the models can be improved by using additional information from the light curve. For example, including the shape of the light curve in several optical and near infrared wavelength bands reduces the scatter to only 15%.

For a given mass of ^{56}Ni, the residual scatter in the model WLR reflects individuating features of the supernova debris structure. The turbulent deflagration phase imprints density and chemical inhomogeneities which lead to variations in the time scale for photons to diffuse out of the debris. In addition, the global asymmetry – due to asymmetric ignition conditions or off-center detonation points – gives rise to anisotropic emission, so that the brightness and duration of most models vary by 20-30% depending of the angle from which they are viewed. While the adoption of a 2-D geometry may exaggerate global asymmetries, spectropolarization observations reveal that SNe Ia typically possess asphericity near or just below the level predicted here[14]. Dimmer supernovae tend to be more polarized, an observation consistent with our finding that dimmer models are more asymmetric due to relatively more burning in the turbulent deflagration phase.

There are both theoretical suggestions[29] and observational indications[30] that the metallicity of the white dwarf will affect the ^{56}Ni yield at the ~10% level. This is because the extra neutrons in trace elements such as ^{20}Ne lead to an increased synthesis of neutronized iron group elements (^{54}Fe and ^{58}Ni) at the expense of ^{56}Ni. To test the first-order effect of metallicity on the light curves, we varied the ^{56}Ni and metal abundances in the ejecta models according to predicted nucleosynthetic results. The resulting light curves (Fig. 4) show that both the peak luminosity and light curve duration decline with metallicity, in a manner roughly consistent with the WLR. Application of the WLR should therefore partially correct for metallicity variations, but with a residual error due to the different slope and normalization of the WLR at different metallicity. For extreme metallicity variations (from 0.3 to 3.0 times the solar value) the error can be as large as 4% in distance. The actual metallicity evolution over the range probed by cosmology experiments is much smaller than this, and we estimate that systematic errors in distance will likely be less than 2%.

The models suggest that a substantial amount of the scatter in the observed WLR arises from the random sub-structures and viewing-angle effects that are predicted by multi-D explosions. In cosmological standard candle applications, these translate to easily reducible statistical errors. On the other hand, additional diversity arises from variations in metallicity and other properties of the progenitor star (e.g., carbon/oxygen ratio, central density, rotation) which may introduce a source of systematic error. Simulation offers one means to test how such variations influence the supernova light curve; for future dark energy experiments this will help to anticipate and limit errors arising from a shift in progenitor demographics over cosmic time.

References

[1] Riess, A. G. et al. Observational Evidence from Supernovae for an Accelerating Universe and a Cosmological Constant. Astron. J., 116, 1009-1038 (1998).

[2] Perlmutter, S. et al. Measurements of Omega and Lambda from 42 High-Redshift Supernovae. Astrophys. J., 517, 565-586 (1999).

[3] Astier, P. et al. The Supernova Legacy Survey: measurement of Ω_M, Ω_Λ and w from the first year data set Astron. Astrophys., 447, 31-48 (2006).

[4] Wood-Vasey, W. M. et al. Observational Constraints on the Nature of Dark Energy: First Cosmological Results from the ESSENCE Supernova Survey. Astrophys. J., 666, 694-715 (2007).

[5] Phillips, M. M., et al. The Reddening-Free Decline Rate Versus Luminosity Relationship for Type IA Supernovae. Astron. J., 118, 1766-1776 (1999).

[6] Höflich, P. et al. Maximum Brightness and Postmaximum Decline of Light Curves of Type IA Supernovae: A Comparison of Theory and Observations. Astrophys. J., 472, L81-L84 (1996).

[7] Pinto, P.A. and Eastman, R.G. The type Ia supernova width-luminosity relation. New Astron., 6, 307-319 (2001).

[8] Kasen, D., & Woosley, S. E. On the Type Ia supernova Width Luminosity Relation. Astrophys. J., 656, 661-665 (2007).

[9] Kuhlen, M., Woosley, S. E., & Glatzmaier, G. A. Carbon Ignition in Type Ia Supernovae. II. A Three-dimensional Numerical Model. Astrophys. J., 640, 407-416 (2006).

[10] Livne, E., Asida, S.M, Hoeflich, P. On the Sensitivity of Deflagrations in a Chandrasekhar Mass White Dwarf to Initial Conditions. Astrophys. J., 632, 443-449 (2005).

[11] Gamezo, V. N., Khokhlov, A.M., and Oran, E.S. Three-dimensional Delayed-Detonation Model of Type Ia Supernovae. Astrophys. J., 623, 337-346 (2005).

[12] Reinecke, M., Hillebrandt, W., and Niemeyer, J. C. Three-dimensional simulations of Type Ia supernovae. Astron. Astrophys. **391**, 1167–1172 (2002).

[13] Livne, E. Delayed Detonation at a Single Point in Exploding White Dwarfs, Astrophys. J., 527, L97-L100, (1999).

[14] Wang, L. and Wheeler, J.C. Spectropolarimetry of Supernovae. Ann. Rev. Astron. Astrophys., 46, 433-474 (2008).

[15] Khokhlov, A. Delayed detonation model for type IA supernovae. Astron. Astrophys., 245, 114-128 (1991).

[16] Hillebrandt, W. & Niemeyer, J. C. Type IA Supernova Explosion Models. Ann. Rev. Astron. Astrophys., 38, 191-230 (2000).

[17] Hoflich, P. and Khokhlov, A., Explosion Models for Type Ia Supernovae: A Comparison with Observed Light Curves, Distances, H_o, and Q_o. Astrophys. J., 457, 500-528 (1996).

[18] Höflich, P., Khokhlov, A. M., and Wheeler, J.C. Delayed detonation models for normal and subluminous type IA sueprnovae: Absolute brightness, light curves, and molecule formation, Astrophys. J., 444, 831-847 (1995).

[19] Kasen, D., Thomas, R. C., & Nugent, P. Time-Dependent Monte Carlo Techniques for the Light Curves, Spectra, and Polarization of Supernovae. Astrophys. J., 651, 366-380 (2006).

[20] Woosley, S. E. et al., Type Ia Supernovae, Jour. Phys. Conf. Ser., 78, 012081 (2007)

[21] Woosley, S.E. Type Ia Supernovae: Burning and Detonation in the Distributed Regime. Astrophys. J., 668, 1109-1117, (2007).

[22] Aspden, A. et al., Turbulence-Flame Interactions in Type Ia Supernovae, Astrophys. J., 689, 1173-1185 (2008).

[23] Woosley, S. E., Kerstein, A., Sankaran, V., and Röpke, F. Type Ia Supernova: Calculations of Turbulent Flames Using the Linear Eddy Model, Astrophys. J. submitted, astroph-0811-3610

[24] Stanishev, V. et al. SN 2003du, 480 Days in the Life of a Normal Type Ia Supernova. Astron. Astrophys., 469, 645-661 (2007).

[25] Hoeflich, P., et al. Signature of Electron Capture in Iron-rich Ejecta of SN 2003du, Astrophys. J., 617, 1258-1266 (2004).

[26] Branch, D., Fisher, A., & Nugent, P. On the Relative Frequencies of Spectroscopically Normal and Peculiar Type Ia Supernovae. Astron. J., 106, 2383-2391 (1993).

[27] Krisciunas, K., Phillips, M. M., & Suntzeff, N. B. Hubble Diagrams of Type Ia Supernovae in the Near-Infrared. Astrophys. J., 602, L81-L84 (2004).

[28] Hamuy, M., et al. The Hubble Diagram of the Calan/Tololo Type Ia Supernovae and the Value of H_O. Astron. J., 112, 2398-2407 (1996).

[29] Timmes, F.X., Brown, E.F., Truran, J.W., On Variations in the Peak Luminosity of Supernovae. Astrophys. J., 590, L83-L86 (2003).

[30] Howell, D.A., et al. The Effect of Progenitor Age and Metallictity on Luminosity and ^{56}Ni Yield in Type Ia Supernovae. Astrops. J., 691, 661-671 (2009).

Received:

Supplementary Information accompanies the paper on **www.nature.com/nature**.

Acknowledgements DNK and SEW thank the Max Planck Institute for Astrophysics for their hospitality during a visit when much of this research was carried out. Support for this work was provided by the DOE SciDAC Program. Support for DNK was provided by NASA through a Hubble fellowship grant awarded by the Space Telescope Science Institute, which is operated by the Association of Universities for Research in Astronomy, Inc., for NASA. The research of F.K.R. is supported through the Emmy Noether Program of the German Research Foundation. We are grateful for computer time provided by NERSC and ORNL through an INCITE award.

Author contributions DNK developed and ran the radiative transfer calculations used to generate synthetic light curves and spectra of the models, and preformed analysis and comparison to observations. FKR setup the initial model conditions and ran the series of hydrodynamical explosion models. SEW provided insight into the parameterization of ignition, detonation, and electron capture, and assisted with the analysis.

Author information The authors declare no competing financial interests. Correspondence and requests for materials should be addressed to DNK (e-mail: kasen@ucolick.org).

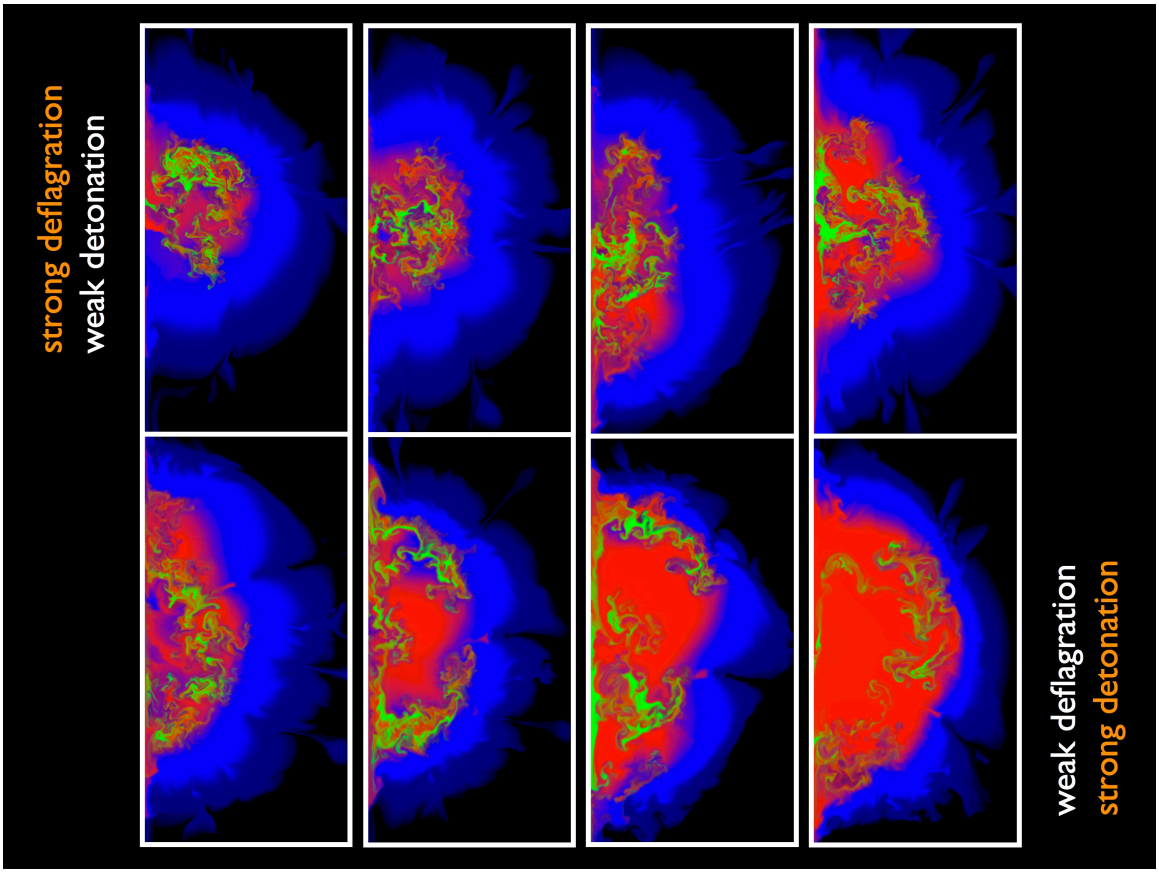

Figure 1: **Chemical structure of the ejected debris for a subset of the explosion models.** Blue represents intermediate mass elements (i.e., silicon, sulfur, calcium), green stable iron group elements produced by electron capture, and red ^{56}Ni. The turbulent inner regions reflect Rayleigh-Taylor and other instabilities that develop during the initial deflagration phase of burning. The subsequent detonation wave enhances the ^{56}Ni production in the center by burning remaining pockets of fuel. The lower density outer layers of debris, processed only by the detonation, consist of smoothly distributed intermediate mass elements.

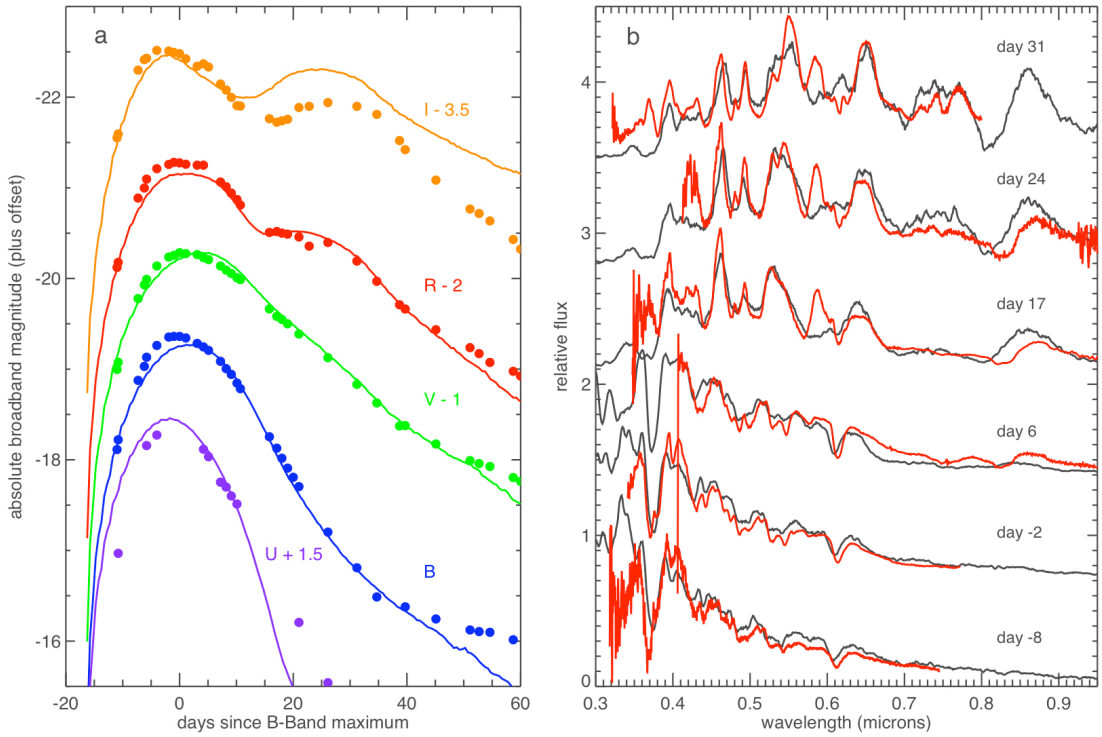

Figure 2: **Synthetic multi-color light curves and spectra of a representative explosion model compared to observations of a normal Type Ia supernova. a.** The angle-averaged light curves of model DFD_iso_06_dc2 (solid lines) show good agreement with filtered observations of SN 20003du (Stanishev et al., 2007; filled circles) in wavelength bands corresponding to the ultraviolet (U) optical (B,V,R), and near infrared (I). **b.** The synthetic spectra of the model (black lines) compare well to observations of SN2003du (red lines) taken at times marked in days relative to B light curve maximum. Over time, as the remnant expands and thins, the spectral absorption features reflect the chemical composition of progressively deeper layers of debris, providing a strong test of the predicted compositional stratification of the model.

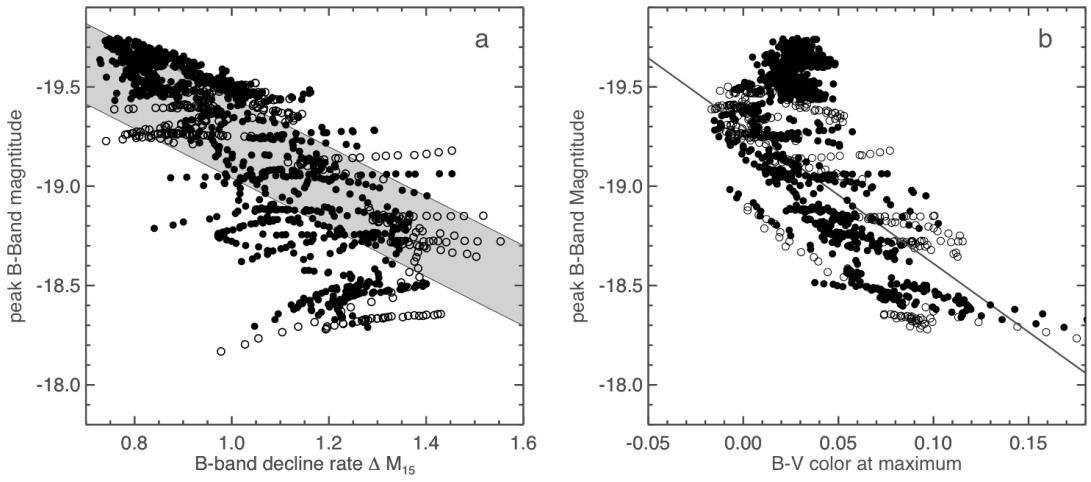

Figure 3: **Correlation of the peak brightness of the models with their light curve duration and color.** The sample includes 44 models each plotted for 30 different viewing angles. Solid circles denote models computed with the most likely range of detonation criteria, while open circles denote more extreme values. **a.** Relation between the peak brightness M_B (measured in the logarithmic magnitude scale) and the light curve decline rate parameter ΔM_{15}, defined as the decrease in B-band brightness from peak to 15 days after peak. The shaded band shows the approximate slope and spread of the observed width-luminosity relation. **b.** Relation between M_B and the color parameter B-V measured at peak. The solid line shows the slope of the observed relation of Philips et al. (1999) but with the normalization shifted, as the models are systematically redder than observed SNe Ia by 7%, likely due to the approximate treatment of non-LTE effects. In observational studies, these two relations are usually fitted jointly as: $M_B = M_{B,0} + \alpha(s-1) + \beta[(B-V)_{\rm Bmax} + (B-V)_0]$, where s is a stretch parameter and $(B-V)_0$ is the color of a fiducial supernova. We take $(B-V)_0 = 0$ and determine stretch using the first order relation: $s = 1 - (\Delta M_{15} - 1.1)/1.7)$. We find for the models fitted values of $\alpha = 2.25, \beta = 4.45$ and $M_{B,0} = -19.27$ which are in reasonable agreement with those derived from the recent observational sample of Astier et al. (2006): $\alpha = 1.52, \beta = 1.57$, and $M_{B,0} = -19.31 + 5\log_{10}(H_0/70)$, where H_0 is the Hubble parameter.

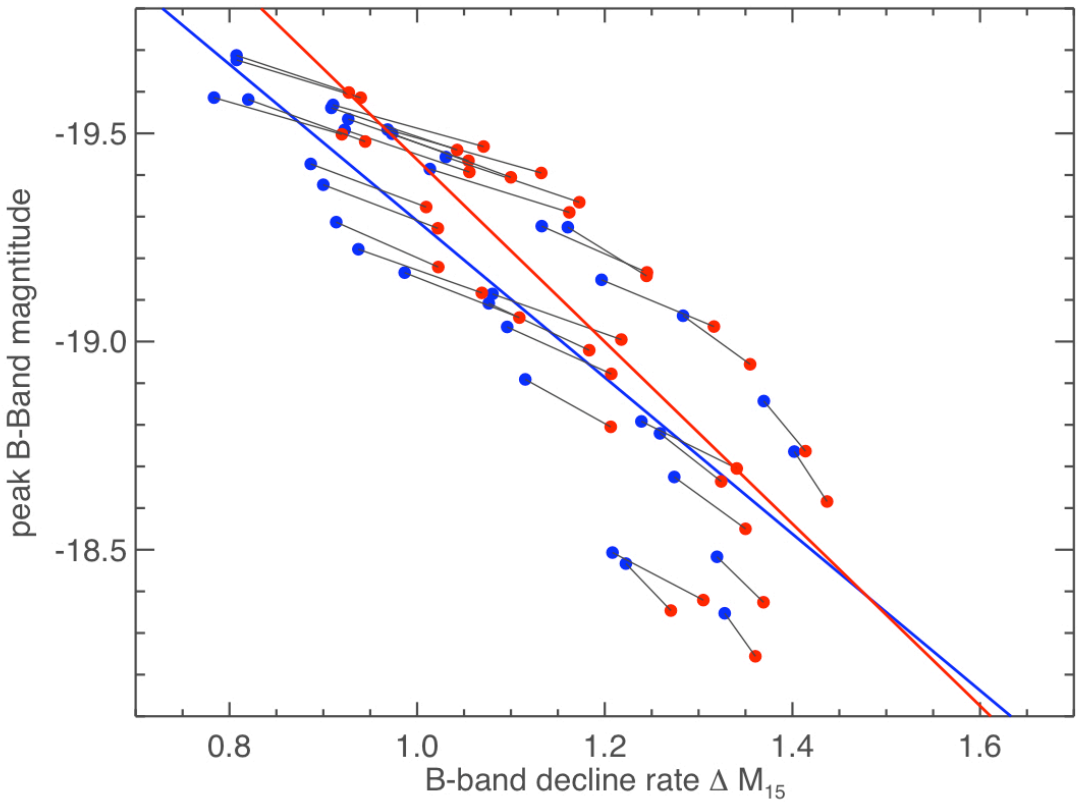

Figure 4: **Effect of the metal content of the progenitor star population on the width-luminosity relation.** The models explore two extreme values of the metallicity: 3 times (red points) and 0.3 times the solar value (blue points). For clarity, each model has been averaged over all viewing angles, and black lines connect similar explosion models of differing metallicity. The colored lines are linear fits to the width-luminosity relation of of the two metallicity samples separately. The diversity introduced by metallicity variations follows the general width-luminosity trend, but the slightly different normalization and slope of the relation for different metallicity samples indicates a potential source of systematic error in distance determinations.

Supplementary Material

1. Explosion Simulations

For simulating the explosion process, we employed a code[12,31,32] that treated the hydrodynamics in a higher-order Godunov scheme[33] and followed the propagation of the thermonuclear flames in a level-set approach[34]. The effects of unresolved turbulence driving the propagation of the deflagration flame were accounted for by a subgrid-scale turbulence model[35]. This approach allowed for a self-consistent treatment of the flame propagation while avoiding tunable parameters.

The deflagration level set was initiated representing a collection of spherical ignition sparks of radius 6 km distributed around the WD center, within a certain solid angle. From 20 to 150 ignition points were considered, randomly distributed from the center out to ~300 km and in a solid angle whose opening varied from 60^{o} to 360^{o}. (see Table 1 for the ignition configurations of each model). Consequently, the ignition region forms a cone with the apex at the center of the WD. Inside this region, the sparks were randomly placed in angular direction. Their distribution in radial direction was randomly drawn from a Gaussian distribution. The apex angles of the cones and the standard deviations of the Gaussian distributions are listed in Table 1.

From these ignition configurations, the deflagration flame fronts evolved subject to buoyancy instabilities on large scales and driven by turbulent motions generated on smaller scales. The deflagration flames propagated from the center of the WD outwards

and released energy, expanding the star. Until getting close to the surface of the WD, the deflagration flame is deformed on large scales by turbulence and thus its propagation is accelerated, but its microscopic structure remains "laminar", with its width and speed determined by radiative diffusion and conduction. Therefore it is stable against detonation. However, as the star expands and the flame burns towards its edge, the density directly ahead of the flame declines. The laminar flame structure becomes thicker and eventually small eddies can penetrate into the burning region and mix hot ash with cold fuel without immediately burning. This mixing process first begins when the Karlovitz number, Ka becomes greater than unity[36], and it has long been speculated that a transition to detonation, were it to happen, would happen here[37]. However, more recent studies[21,22] suggest that the first structures to form at the transition to distributed burning are too small to detonate. Greater mixing, and therefore a lower density and higher Karlovitz number are required. The largest mixed structures are formed when the eddy turnover time on the integral scale for the turbulence is equal to the nuclear burning time for the mixture, i.e., Damköhler number ~ 1. The effects of intermittency will raise this value some[38] to perhaps Da ~ 10. Estimating the nuclear time scale with a small reaction network and assuming turbulent energies appropriate to the supernova[39], this corresponds to Ka ~ 500.

This possibility of a deflagration-to-detonation transition (DDT) was implemented in the models by determining Ka in each zone near the flame surface based upon the turbulent energy as derived from the subgrid-scale turbulence model. Here Ka is defined as Ka = $(\delta/L_{Gib})^{1/2}$ where δ is the laminar flame width, and the Gibson length, L_{Gib} =

$[S_{lam}/u'(\Delta x)]^3 \Delta x$, with S_{lam}, the laminar flame speed and u', the turbulent *rms* fluctuation speed on the scale of the computational grid Δx. For a DDT to occur in our simulation, we required a minimal Karlovitz number and a certain range of fuel densities ahead of the flame, as given in Table 2. We considered five different values of critical Karlovitz number. Most models used a value in the most physically plausible range (Ka = 250, 750) while other models explored more extreme values (Ka = 1, 1500, 2250).

Once the flame fronts reached the critical conditions for detonation, a level set representing a detonation was initiated at the corresponding location. If other features of the flame reached critical DDT conditions, further detonations were initialized there on the basis of the same level set. Thus, a sequence of DDTs was possible and indeed realized in all models. The detonation level set was then propagated with an appropriate detonation velocity[40], exhausting most of the remaining fuel. The level-set treatment of the detonation allowed us to prevent it from unphysically crossing ash regions left behind by the preceding deflagration phase.

Each thermonuclear supernova explosion model is now specified by one of the deflagration ignitions configurations listed in Table 1 and one of the DDT conditions of Table 2. In total, 44 models were computed.

Depending on the fuel density ahead of the flame, the C+O material of the WD was converted to a nuclear statistical equilibrium composition (NSE; modeled as a temperature-and density-dependent mixture of ^{56}Ni and alpha-particles), or to

intermediate mass elements (modeled by a representative nucleus of A=30 and a nuclear binding energy of 8.17906×10^{18} erg g^{-1}), or to oxygen. Electron captures in the NSE were accounted for in a parameterized way allowing us to differentiate radioactive ^{56}Ni from stable iron group elements.

For select models, we carried out detailed post-processing nucleosynthesis calculations using Lagrangian tracer particles and a full nuclear network (see Figure 1 for two models discussed in the main text). For one of the more representative models (D2D_iso_06_dc1) we tabulated the detailed compositions comprising each of the coarse groups followed in the explosion calculations. These tables were used for the remaining models to interpolate the abundances of all elements, a prerequisite for the spectrum synthesis modeling described below. The light curves are less sensitive to the details of the abundance interpolation.

The explosion simulations were run in cylindrical (r-z) geometry and a spatial resolution of 512x1024. Imposing rotational symmetry along the z-axis, the full star was represented in this two-dimensional setup. The hydrodynamical evolution of each model was followed for 100 seconds, well after burning had ceased and at which point the gravitational and internal energy densities were small (< 1%) relative to the kinetic energy density. At this time, the velocity structure was homologous (velocity proportional to radius) to better than a percent, indicating that the remnant had reached the phase of free-expansion.

The explosion models all assumed the progenitor star had solar metallicity. To explore how varations in metallicity may influence the light curve, we changed the composition of the debris structure in each explosion model to reflect certain nucleosynthetic results. Timmes[29] showed in an analytical calculation that a higher metallicity leads to a greater production of stable iron group elements (^{54}Fe and ^{58}Ni) at the expense of ^{56}Ni. We therefore varied the ^{56}Ni mass according to $M_{ni}(Z) = M_{ni}(Z=1) * (1 – 0.057 (Z-1))$, where the metallicity was changed to Z = 3 and Z = 0.3 times solar. The trace abundance of metals in unburned or partially burned material, which has some influence on the ejecta opacity, was also changed to reflect the progenitor metalicity. This approach does not account for the effect metallicity may have on the structure of the white dwarf, or on the dynamics of the explosion.

2. Radiative Transfer Calculations

Light curves and spectra of the models were computed using the multi-wavelength time-dependent radiative transfer code SEDONA[19], which uses a Monte Carlo approach to solve the transport equation in arbitrary geometries. The final structure of each explosion model described above was remapped to a lower resolution (64x128) regular cylindrical grid to provide the initial conditions for the transfer code. SEDONA assumes the subsequent dynamics are given by homologous expansion and self-consistently calculates the temperature structure evolution by balancing sources of radiative heating and cooling.

The light curves of SNe Ia are powered by the radioactive chain ^{56}Ni -> ^{56}Co -> ^{56}Fe. The decay releases primarily ~1 MeV gamma-rays, which deposit their energy in the

ejecta mainly through Compton scattering and photo-electric absorption. The SEDONA code includes a detailed multi-wavelength transport scheme treating the emission, propagation, and absorption of gamma-rays. This provided the instantaneous rate and geometry of radioactive energy deposition, as well as predictions for the emergent gamma-ray light curves and spectra.

Absorbed radioactive energy was assumed to be locally and instantaneously reprocessed into optical/UV photons, whose propagation was followed using a Monte Carlo method. Detailed non-grey opacities were applied, including the aggregate effects of over 10 million bound-bound line transitions[41] treated in the expansion opacity formalism[42]. Atomic level populations were calculated assuming local thermodynamic equilibrium (LTE), typically a reasonable approximation for SNe Ia in the earlier epochs[43]. The radiation field, on the other hand, was not required to be in LTE, and an equivalent two-level equivalent atom (ETLA) formalism was used for the line source function: $S = (1 - \varepsilon) J + \varepsilon B$, where ε is the ratio of absorptive opacity to total (scattering plus absorptive) opacity. A constant value $\varepsilon = 0.3$ was used for all lines to approximate non-LTE effects based on comparison to previous line branching calculations.

The most significant uncertainties in the light curve calculations relate to uncertainties in the calculation of the complex opacities/emissivities, in particular the likely inaccuracy and/or incompleteness of the atomic line database, and the limitations of the expansion opacity and ETLA formalisms. In the future, self-consistent multi-dimensional non-LTE calculations will help refine the quantitative accuracy of the models.

.

References

[31] Röpke, F. K., Following multi-dimensional type Ia supernova explosion models to homologous expansion. Astron. Astrophys. 432, 969–983 (2005).

[32] Röpke, F. K., and Niemeyer, J. C. Delayed detonations in full-star models of type Ia supernova explosions. Astron. Astrophys. 464, 683–686 (2005).

[33] Fryxell, B. A., and Müller, E. Hydrodynamics and nuclear burning. MPA Green Report 449 (1989).

[34] Reinecke, M., Hillebrandt, W., Niemeyer, J. C., Klein, R., and Gröbl, A. A new model for deflagration fronts in reactive fluids. Astron. Astrophys. 347, 724–733 (1999).

[35] Niemeyer, J. C., and Hillebrandt, W. Turbulent Nuclear Flames in Type Ia Supernovae. Astrophys. J. 452 769–778 (1995).

[36] Peters, N. in Turbulent Combustion, Cambridge Univ. Press, p. 78 (2000).

[37] Niemeyer, J. C., and Woosley, S. E., The Thermonuclear Explosion of Chandrasekhar Mass White Dwarfs, Astrophys. J., 475, 740–753, (1997).

[38] Pan, L., Wheeler, J. C., and Scalo, J., The Effects of Turbulent Intermittency on the deflagration to Detonation Transition in Type Ia Supernova Explosions, Astrophys. J., 681, 470–481 (2008).

[39] Röpke, F. Flame Driven Deflagration to Detonation Transitions in Type Ia Supernovae, Astrophys. J., 668, 1103–1108 (2007).

[40] Golombek, I., and Niemeyer, J. C. A model for multidimensional delayed detonations in SN Ia explosions. Astron. Astrophys. 438, 611–616 (2005).

[41] Kurucz, R. Atomic Data for Opacity Calculations, CD-ROM 1, Cambridge: Smithsonian Astrophysical Observatory (1993).

[42] Eastman, R., and Pinto, P. Spectrum Formation in Supernovae: Numerical Techniques. Astrophys. J., 412, 731-751 (1993).

[43] Baron E., Hauschildt, P., Nugent, P., and Branch, D. Non-local Thermodynamic Equilibrium Effects in Modeling of Supernovae near Maximum Light. Mon. Not. R. Astron. Soc., 283, 297-315 (1996).

Table 1: Deflagration ignition configurations. The half apex angle of the cone centered on the WD in which the ignition is assumed to take place is denoted by α.

Ignition setup	Number of ignition kernels	Minimal distance of kernels [kernel radii]	cos(α)	Standard deviation [km]
DD2D_iso_01	20	1.0	-1.0	150.0
DD20_iso_02	50	0.8	-1.0	150.0
DD2D_iso_03	60	0.7	-1.0	150.0
DD2D_iso_04	80	0.8	-1.0	150.0
DD2D_iso_05	90	0.7	-1.0	150.0
DD2D_iso_06	100	0.1	-1.0	150.0
DD2D_iso_07	100	0.5	-1.0	150.0
DD2D_iso_08	150	0.3	-1.0	150.0
DD2D_asym_01	120	0.3	-1.0	75.0
DD2D_asym_02	105	0.3	-0.75	75.0
DD2D_asym_03	90	0.3	-0.50	75.0
DD2D_asym_04	75	0.3	-0.25	75.0
DD2D_asym_05	60	0.3	0.0	75.0
DD2D_asym_06	45	0.3	0.25	75.0
DD2D_asym_07	30	0.3	0.50	75.0
DD2D_asym_08	15	0.3	0.75	75.0

Table 2: Criteria for deflagration-to-detonation transitions

DDT criterion (dc)	Ka_{min}	ρ_{min} [10^7 g cm^{-3}]	ρ_{max} [10^7 g cm^{-3}]
1	1.0	0.6	1.75
2	250.0	0.6	1.20
3	750.0	0.6	1.20
4	1500.0	0.6	1.20
5	2250.0	0.6	1.20